Thermal Science and Engineering Progress 38 (2023) 101659

Contents lists available at ScienceDirect

Thermal Science and Engineering Progress

journal homepage: www.elsevier.com/locate/tsep

Design space analysis for supercritical CO_2 radial inflow turbine stators

Jianhui Qi [a,b,c,*], Yueming Yang [a], Kuihua Han [a], Ming Gao [a], Yingjie Li [a], Suoying He [a], Jinliang Xu [b]

[a] School of Energy and Power Engineering, Shandong University, Jinan 250061, China
[b] Beijing Key Laboratory of Multiphase Flow and Heat Transfer for Low Grade Energy Utilization, North China Electric Power University, Beijing, 102206, China
[c] Suzhou Research Institute, Shandong University, Suzhou 215123, China

ARTICLE INFO

Keywords:
Radial inflow turbine
Nozzle guide vanes
One-dimensional model
Design space analysis
CFD simulation

ABSTRACT

Radial inflow turbines(RITs) play a vital role in power generation due to their small size, compact construction and large power density, especially when applying to supercritical CO2(sCO_2) power cycles. Correct preliminary design of the RITs is important for enhancing the efficiency of cycles. Most preliminary design studies for RITs simply impose empirically developed angle constraints for the rotor inlet conditions instead of giving much attention to the stators. In addition, the previous design procedure can only calculate one geometry at a time, which does not allow the selection of the most suitable geometry that fits the cycle parameters and constraints. Hence, this paper presents a workflow to correctly size a stator for achieving a desired rotor inflow conditions. Then a stator design-space analysis with utilising an existing 500 kW sCO_2 rotor is conducted. Based on a number of given stator radius ratio(r_3/r_4), blade number(Z_s) and blade trailing edge thickness(t_3), the obtained design map contains a total number of $N_{r_3/r_4} \times N_{Z_s} \times N_{t_3}$ preliminary design cases. New insights are discussed, including that the workflow is functional; the blade angles need to adjust between no-loss and loss cases; the rotor–stator interaction loss will increase the stator inlet/outlet operational parameter when guaranteeing the target rotor inlet conditions; and including of the stator losses in turbine design is significant.

1. Introduction

Problems associated with the fast development of human society, such as climate change, environmental pollution, and global warming, have created an international drive towards renewable energy utilisations [1]. There are different kinds of renewable energy resources available on earth. Solar energy is the most abundant, and it has already been used by human society in various forms since ancient times [1]. The global solar energy potential is estimated at 1575 EJ to 49 837 EJ per annum, many times the size of human kinds of energy consumption [2]. Nevertheless, current solar energy is only a comparatively small contributor to the overall energy mix. One of the causes of low uptake is the limited dispatchability of solar energy. Solar energy is only generated when the sun is out and storing electricity is still expensive, albeit battery costs have been reducing in recent years.

Concentrating solar power (CSP) in conjunction with thermal storage is well suited to address this problem. CSP systems capture solar energy and convert it to thermal energy, which can be stored cheaply and converted into electric energy using heat engines when demand exists. CSP systems have a crucial advantage over Photo Voltaic (PV) + batteries system, indicating cheap thermal storage media and cheap storage systems (typically tanks). This key advantage has attracted more and more attention recently [3].

Normally the CSP can use steam Rankine cycles or open Brayton gas turbine cycles. Steam Rankine cycles suffer from the significant loss of low-grade thermal energy at the condenser because the cycle relies on condensation in order to be able to pump water [4]. Open-cycle gas turbines have no cooling loss but use approximately 45% of the power produced by the high-temperature expansion in compressing air, along with considerable heat loss in the exhaust. Both of them suffer efficiency losses when used by CSP applications.

A high-efficiency power cycle receiving considerable interest at present by all sectors of the power industry is the supercritical $CO2_2$ (sCO_2) Brayton cycle [4]. As reported in study [5], a reduction of 8% levelised cost of electricity is estimated to be achieved by replacing the steam Rankine cycle with a sCO_2 power cycle in the existing molten salt tower power plant. For this reason, the sCO_2 power cycle is considered a promising solution for CSP systems.

Feher [6] has presented the concepts of a supercritical power cycle and designed the first sCO_2 power cycle in 1968. Recent works [7,8] have shown that cycle efficiencies above 50% are achievable, even

* Corresponding author at: School of Energy and Power Engineering, Shandong University, Jinan 250061, China.
E-mail address: j.qi@sdu.edu.cn (J. Qi).

https://doi.org/10.1016/j.tsep.2023.101659
Received 16 May 2022; Received in revised form 27 December 2022; Accepted 6 January 2023
Available online 18 January 2023
2451-9049/

Nomenclature

Acronyms

CSP	Concentration solar power.
NGVs	Nozzle guide vanes.
RIT	Radial inflow turbine.
sCO_2	Supercritical carbon dioxide.

Greek Symbols

α	Absolute flow angle, [°].
β	Relative flow angle, [°].
δ	The nozzle guide vanes incline angle, [°].
δ'	Displacement thickness, [m].
γ	Gas constant, [-].
Φ	The objective function.
ϕ	Helmholtz energy.
ψ	Energy thickness, [m].
ρ	Flow density, [$\mathrm{kg\,m^{-3}}$].
θ	Centre angle, [°].
θ'	Momentum thickness, [m].
1D, 2D, 3D	One-, two-, three-dimensional.

Roman Symbols

$\dot{m}$	Mass flow rate, [$\mathrm{kg\,s^{-1}}$].
$\mathbf{V}$	State vector.
A	Actual flow area, [$\mathrm{m^2}$].
b	Blade height, [m].
C	Absolute flow velocity, [$\mathrm{m\,s^{-1}}$].
d	Diameter, [m].
E	Energy factor.
e	Nozzle guide vanes loss coefficient.
H	Absolute enthalpy, [kg K].
h	Passage height, [m].
L_t	Throat width, [m].
M	Flow Mach number, [-].
p	Flow static pressure, [Pa].
r	Radius, [m].
S	Pitch curve length, [m].
s	Nozzle guide vanes blade spacing at blade-row exit, [m].
T	Static temperature, [K].
t	Blade edge thickness, [mm].
Z	Blade number, [-].

Subscripts

0	Stagnation condition.
1	Stator inlet section.
1	Stator inlet.
3	Stator outlet section.
4	Rotor inlet section.
b	Blade.
c	Calculated value.
i	Interspace section.
R	Radial component.
r	Rotor.
s	Stator.
T	Tangential component.
t	Target value.
ti	The tip of the blade.

in conjunction with dry cooling, making sCO_2 power cycle ideal for CSP plants that are most commonly sited in arid locations. Further advantages of sCO_2 over other working fluids, such as steam, are its ability to effectively utilise compact recuperation and lower cycle pressure ratios. These advantages allow for higher average temperatures in the heater, which brings about increasing efficiencies and fewer stages in the turbomachinery components and allows turbines to package in single casings or the use of single-stage expanders, further decreasing cost.

A study by Allison et al. [9] compares the efficiency of a high-temperature (700 °C) simple Brayton cycle configuration concerning a range of compressors and turbine efficiency. The results show that every 2% increase in turbine efficiency brings about approximately a 1% increase in cycle efficiency, while every 2% increase in compressor efficiency brings about approximately a 0.5% increase in cycle efficiency. Similarly, Cho et al. [10] has pointed out that turbine efficiency has more effect on the overall thermal efficiency. As the turbine is the most critical rotating component, it must be selected and designed carefully to reach an exceptional performance.

Due to lower pressure ratios and the highly dense working fluid, Radial Inflow Turbines (RITs) are a good solution for sCO_2 power cycles. Their advantages are easy to manufacture, low cost, and compact construction [11], especially for the power scale less than 30 MW [12]. Many researchers [13–16] have presented various design methodologies for RITs. These procedures are focused on solving the fundamental turbomachinery equations, predicting the fluid properties, and calculating the rotor efficiency through well-developed loss models, and allow the designer to match the turbine design with the cycle requirements and vice versa.

The sCO_2 turbine designs are characterised by high specific work outputs and operation at low specific speed [1,17]. For such designs with high rotor inlet swirls, nozzle guide vanes (NGVs) are essential [16]. However, most preliminary design studies for sCO_2 RITs simply impose empirically developed angle constraints for the rotor inlet flow conditions instead of giving much attention to the stator, as some researchers recognise that the losses in stator can be ignored [16,18,19]. Some stator design models, such as the models used to determine the blade numbers, the blade chords, etc., are presented in Appendix C.

Hence, the typical preliminary design process of RITs are focus on designing the rotor first, such as the process provided by Moustapha et al. [16], and the in-house RIT design code `TOPGEN` [1,20]. Then, based on a priori-designed rotor geometry, the value of the parameters to define a stator will be recommended directly based on very simple correlations.

Nevertheless, this design process is only feasible for turbines operating with air or steam, i.e. low density fluids. For sCO_2 or other high-pressure ratio turbines, a large deviation at the rotor inlet section between the real and designed case will be generated. The reason for deviations are accounted for two reasons. Firstly, the studies of Keep et al. [17] and Wheeler et al. [21] have indicated that the stator losses are a substantially larger contributor to losses in sCO_2 and ORC turbines than some of the traditional design methods claim (e.g. Rholik model [13]), especially when the stator works on large pressure ratio with supersonic flow conditions. For example, as shown in the work by Keep et al. [17], about 50% of total loss (consume about 13% of total enthalpy difference across the stage) are generated at stator section for a 300 kW sCO_2 radial turbine. Then, Simple stator design correlations cannot guarantee the rotor inlet conditions.

What is more, based on an already designed rotor, recommended values of defining a stator, are given in Table 1, with corresponding

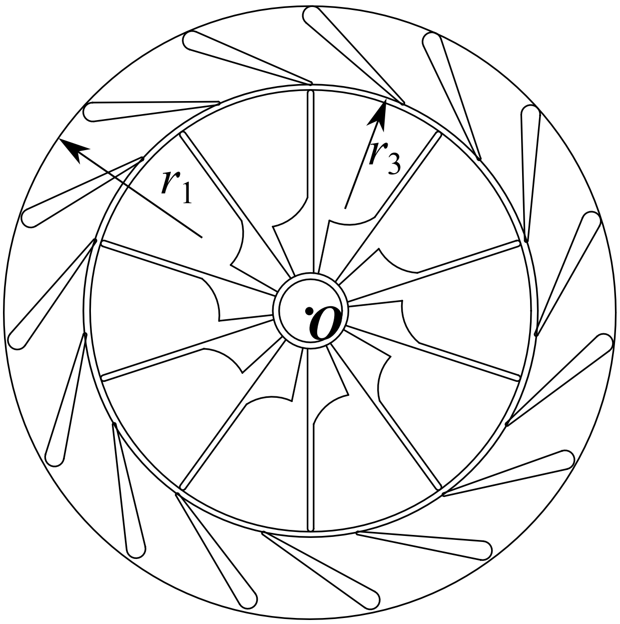

Fig. 1. Schematic of a RIT with nozzled stator.

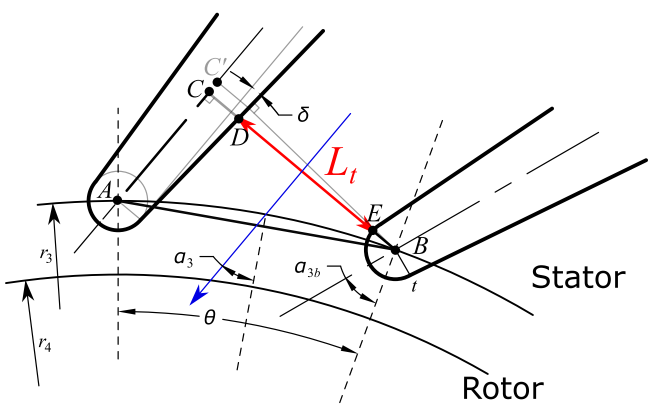

Fig. 2. Detailed stator outlet geometry.

geometric parameters defined in Figs. 1 and 2. These constraints have been developed to respect the physical limitations (e.g. blade vibrations, machining limits, etc.) and to ensure good performance, which is drawn from experience in turbines operating with conventional fluids. While fundamentally the same constraints still exist in sCO_2 turbines, the ramifications of such constraints as the shift to highly dense fluid, smaller geometric dimensions, and lower specific speeds (typically for single stage RITs with power outputs less than 30 MW [12]) have become different. These constraints imply that different areas of the design spaces may become feasible, providing avenues to enhance performance, while traditional stator designs may fail at the constraints. To meet the above requirements, designers need the ability to rapidly explore what stator geometries deliver the desired rotor inflow conditions, as well as an awareness of the feasible stator design space and how this is impacted by constraints.

Based on the aforementioned discussion, the objective of this paper is twofold. First, we present a methodology to correctly size a stator, so as to achieve the desired rotor inflow condition during the preliminary design stage. This approach is verified against sCO_2 stage simulations at a relevant scale. Second and the most important, we conduct a stator design space analysis by utilising an existing 500 kW sCO_2 turbine

Table 1
Empirical constraints for a small RITs stator NGVs preliminary design.

Item	Constraint
r_1	$r_3 + 0.2 \cdot r_4$ [a]
r_3	$r_3 > 10 \times 10^{-3}$ m [b]
	$r_3/r_{6t} > 1.42$ [18]
b_3	$b_3/r_4 > 0.04$ [18]
b_4	$b_4 > 2.0$ mm [18]
α_3	65 to 80° [18]
β_3	−40 to −20° [19,22]
t	0.9 mm [c]

[a] This is a recommended value [16].
[b] Under the condition that there is no gap between stator outlet and rotor inlet [18].
[c] For vanes with a low blade height ($b_3 < 2$ *to* 3 mm) [18].

rotor. Analysing feasible stator geometries that achieve the desired rotor inflow conditions in the context of empirical constraints listed in Table 1, allows deductions to be made about preferred stator designs and the impact of stator and interspace losses.

The paper is constructed with the following sections: Section 2 develops and verifies the stator sizing methodology. Section 3 adopts a candidate 500 kW sCO_2 RIT rotor design to conduct a design space exploration and to elucidate preferred design choices. Finally, Section 4 gives a brief conclusion and outlines future work.

2. Methodology

At beginning of the preliminary design stage, all the rotor inlet geometry (r_4, A_4, b_4, t_4, Z_r) and flow conditions (α_4, p_4, T_4, M_4), etc., are directly obtained by RIT in-house preliminary design code TOP-GEN [1,18]. However, without properly designed stator NGVs, these rotor inlet conditions are hardly reached. In this section, a methodology will be developed to obtain the stator NGVs exit geometrical (r_3, A_3/b_3, t_3, Z_s) and flow (p_3, T_3, M_3, α_3) properties, under which the given set of rotor inlet conditions can be really achieved. The corresponding stator NGVs exit geometrical and flow properties are defined in Fig. 2. Then the method to present a stator design space will be developed.

2.1. Overview of the methodology

To obtain the designed stator, some parameters are important to be considered, that the stator–rotor interspace size, defined by the radius ratio, r_3/r_4, the blade opening size, related to the stator blade number Z_s, and the trailing edge thickness, t_3. Hence, to generate the stator NGVs outlet parameters, we need to set the three geometrical parameters first.

The workflow can be described as:

1. The given set of rotor parameters are used as the desired target value (marked with subscript 't'), i.e. the value can be obtained with correctly design NGVs exit geometrical and flow conditions.
2. Three stator constraints, nozzle exit to rotor radius ratio($\frac{r_3}{r_4}$), number of blades (Z_s), stator trailing edge thickness (t_3), and the stator half-angle (δ) (For automated design space evaluations, the constraints can be replaced by ranges) are set.
3. Initial guess stator exit flow conditions (M_3, p_3, α_{3b}).
4. With the constraints and the guessed flow conditions, the rest stator parameters can be derivated.
5. Conservation equations are iteratively solved to get the calculated rotor inlet values (marked with subscript 'c').
6. The equation solver updates the guessed stator exit flow conditions until the calculated rotor inlet values match the target value.
7. Return the stator exit conditions (geometric and flow) and store them in a data table.

Fig. 3 shows the workflow we employ. To aid this description, Fig. 2 shows the schematic of the stator outlet geometry. In this schematic, the trailing edges of two stator NGVs are plotted, which form a convergent subsonic nozzle (in this study, only the convergent subsonic nozzle is considered).

The following sections describe the stator geometry construction, the models used to construct all the stator geometrical and flow parameters are presented. Then, isentropic governing equations linking stator exit and rotor inlet properties are proposed. Next, to deal with the effect of losses, lumped-parameter loss models are introduced. Next, the numerical method used to solve the governing equations and update the guessed flow properties is introduced. Finally, the method to generate the stator design spaces is shown.

2.2. Models to connect stator geometry and flow properties

During the conservation equation solving process, the calculation starts from the current estimates of the stator outlet conditions, namely, M_3, p_3, and α_{3b}. By using these values and the constraints $\frac{r_3}{r_4}$, Z_s, t_3, and δ, the remaining stator outlet parameters (as shown in Fig. 2) are calculated as follows.

We start by calculating the effective stator throat width, L_t. According to Fig. 2,

$$AB = 2r_3\cos\left(\frac{\pi}{2}-\frac{\theta}{2}\right) = 2r_3\sin\frac{\theta}{2} = 2r_3\sin\frac{\pi}{Z_s}\ . \tag{1}$$

The NGVs are assumed to be thickening with an angle δ, which occurs on both sides of the vanes. In this context, the value of δ must be positive to avoid inward curve of the vane shape. As δ is small, the length $BC' = \cos\delta\, BC \approx BC$. Thus BC can be calculated with

$$BC = \cos\left(\alpha_{3b}-\frac{\pi}{Z_s}\right)AB\ . \tag{2}$$

And the remaining dimensions are given by

$$AC = \sin\left(\alpha_{3b}-\frac{\pi}{2}\right)2\,r_3\sin\frac{\pi}{Z_s} \tag{3}$$

$$DC = r_t + AC\tan\delta \tag{4}$$

$$BE = r_t \tag{5}$$

Thus L_t is calculated as

$$L_t = BC - BE - DC\ . \tag{6}$$

Once stator throat width is known, α_3 can be calculated based on the cosine correlation, given by [23]:

$$\alpha_3 = \cos^{-1}\left(\frac{L_t}{S_3}\right)\ , \tag{7}$$

with

$$S_3 = \frac{2\,\pi\, r_3}{Z_s}\ . \tag{8}$$

In reality, this α_3 may be slightly different from what is shown in Fig. 4. As the flow goes across the stator exit plane, the sudden expansion will cause a slight change in the main flow angle. As we are focused on the design of sub-sonic stator and quasi 1D models are applied, this change of angle is neglected to simplify the calculation.

Then, the flow area A_3 can be calculated:

$$A_3 = \left[2\pi r_3 - Z_s\, r_t\left(1+\frac{1}{\cos\alpha_{3b}}\right)\right] b_3 \tag{9}$$

By using these relations, we can use the geometric constraints to calculate the remaining geometry and flow properties as shown in Fig. 2. The calculation models for solving the flow properties are shown in Appendix A.

- Constraints: $\frac{r_3}{r_4}$, Z_s, t_3, δ
- Calculated: r_3, α_{3b}, L_t, S_3, A_3

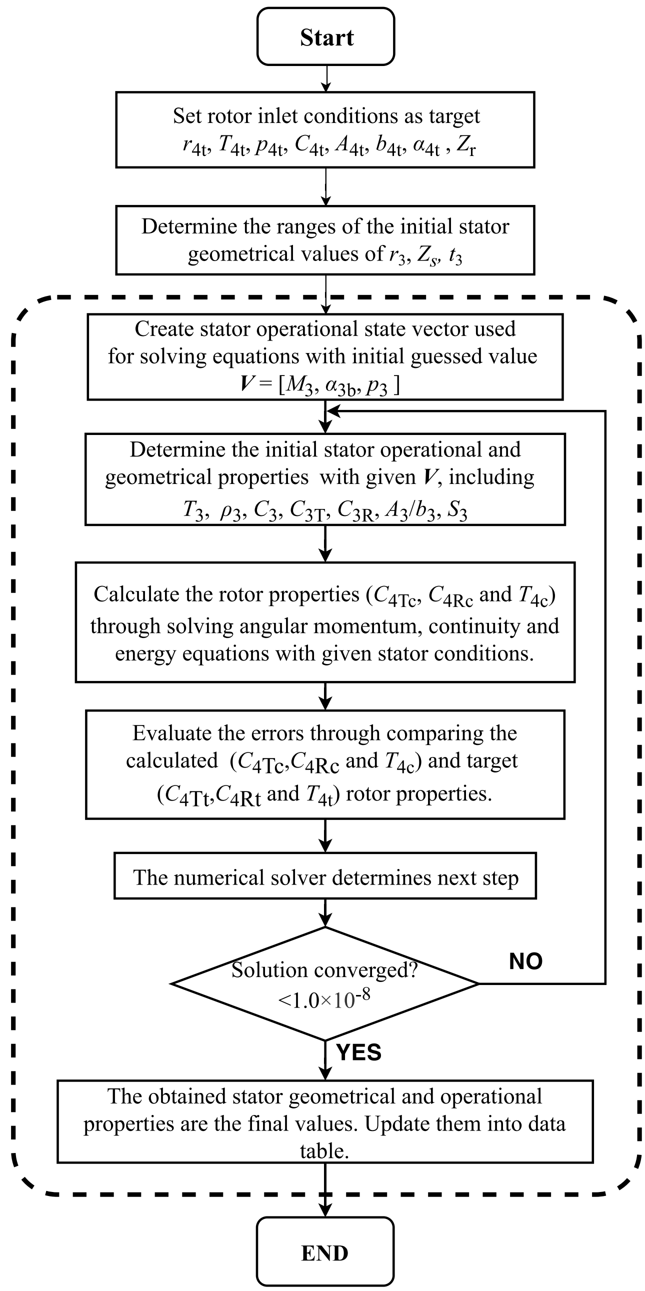

Fig. 3. The flow chart of the calculation process.

- Flow properties: M_3, α_3, p_3, T_3, ρ_3, p_{03}, T_03, h_3, a_3, s_3

Once address all the stator properties, the relations between stator and rotor properties are needed to calculate the rotor inlet condition.

2.3. Relations between stator and rotor properties

To better applied with equation solvers, the relations between stator and rotor properties are separated with isentropic term and loss term. The loss terms are total pressure loss factor, η_p and momentum loss factor, η_q, which will be discussed in follows. Then, the conservation equations for mass, angular momentum, and energy can be used to obtain flow conditions to relate fluid properties at the stator exit (marked with subscript 3) and rotor inlet (marked with subscript 4). The equations are:

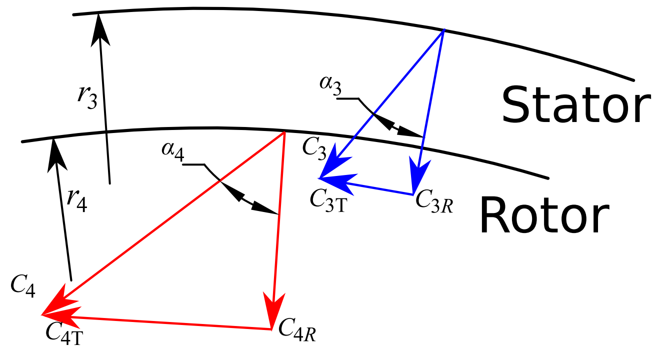

Fig. 4. The velocity triangles of the stator and rotor.

- Conservation of total energy between the stator outlet (h_{03}) and rotor inlet (h_{04}). Hence,

$$h_{03} = h_{04} \,,$$
$$\boldsymbol{f}_h(T_3, p_3) + \frac{1}{2} C_3^2 = \boldsymbol{f}_h(T_4, p_4) + \frac{1}{2} C_4^2 \,, \tag{10}$$

where $\boldsymbol{f}_h(T, p)$ is a function to obtain static enthalpy as defined in Appendix A.

- For continuity, we assume there is no loss of mass flow from the interspace. Hence,

$$\dot{m}_3 = \dot{m}_4 \,, \tag{11}$$
$$C_{3R}\, \rho_3\, A_3 = C_{4R}\, \rho_4\, A_4 \,,$$
$$C_{3R}\, \boldsymbol{f}_\rho(T_3, p_3)\, A_3 = C_{4R}\, \boldsymbol{f}_\rho(T_4, p_4)\, A_4 \,, \tag{12}$$

where $\boldsymbol{f}_\rho(p, T)$ is an equation to obtain density defined in Appendix A.

- For conservation of angular momentum, we include a loss factor (η_q) so that angular momentum loss can be incorporated. The resulting angular momentum equation is,

$$\left(1 - \eta_q\right)\; \dot{m}_3\, C_{3T}\, r_3 = \dot{m}_4\, C_{4T}\, r_4 \,. \tag{13}$$

Using Eq. (11) to eliminate $\dot{m}$ yields

$$\left(1 - \eta_q\right)\, C_{3T}\, r_3 = C_{4T}\, r_4 \,. \tag{14}$$

Furthermore, the flow angles and velocity components are related through the velocity triangles shown in Fig. 4, allowing the radial and tangential components to be linked to the absolute velocity

$$C_{4Rc}^2 + C_{4Tc}^2 = C_{4c}^2 = M_{4c}^2\, a_{4c}^2 \,. \tag{15}$$

The above equations are solved by considering the loss of total pressure and employing a suitable equation of state (EoS). The total pressure loss between stator outlet and rotor inlet is defined by using a total pressure loss factor η_p:

$$\left(1 - \eta_p\right)\, p_{03} = p_{04} \,. \tag{16}$$

Then the equation is expanded to

$$\eta_p \left(p_3 + \frac{1}{2}\, \rho_3\, C_3^2\right) = p_{4c} + \frac{1}{2}\, \rho_{4c}\, C_{4c}^2 \,, \tag{17}$$
$$\eta_p \left(p_3 + \frac{1}{2}\, \boldsymbol{f}_\rho(p_3, T_3)\, C_3^2\right) = p_{4c} + \frac{1}{2}\, \boldsymbol{f}_\rho(p_{4c}, T_{4c})\, C_{4c}^2 \,. \tag{18}$$

The method about the loss factors are given in detail in Section 2.4, and the value will be selected in Section 4.3.

The solution process first uses Eqs. (12) and (14) to eliminate C_{4Tc} and C_{4Rc} from Eq. (15). Then the resulting equation is used to eliminate C_{4c} from Eqs. (10) and (17) respectively, yielding two equations with pressure (p_{4c}), temperature (T_{4c}), and density (ρ_{4c}) as the remaining unknown variables. The resulting two simultaneous equations, together with the EoS can be solved numerically to find pressure, temperature and density, and once these parameters are known, the remaining outlet conditions can be recovered.

The equations developed to this point are true both for ideal and non-ideal gases, details are presented in Appendix A.

By adopting these relations, we can use the flow conditions at the stator exit to estimate the corresponding rotor inlet conditions.

- Inputs flow: p_3, T_3, C_3, α_3
- Inputs geometry: α_{b3}, r_3, L_t, S_3, A_3
- Outputs: p_{4c}, T_{4c}, C_{4R}, C_{4T}

2.4. Accounting for losses

As addressed in the introduction section, the loss models that were developed previously may not be adequate for sCO_2 applications. Hence, in this section, lumped-parameter loss models are developed to assist analysis of the effect of stator loss on the design space.

Solving the above equations without losses, $\eta_p = 0$ and $\eta_q = 0$ result in an isentropic process for the flow from the stator outlet to the rotor inlet. This provides the ideal scenario, and can be used to analyse the design trends theoretically, but losses are presented at the stator exit and in the rotor–stator interspace in practice. Once the analysis of losses is needed, the lumped-parameter loss term can be set to a value larger than zero, i.e. $\eta_p > 0$ and $\eta_q > 0$. Typically these losses arise from the following mechanisms,

1. Profile loss [19], which arises due to skin friction on the stator blade surface, causing the formation of the boundary layer. These manifest as a loss of total pressure;
2. Trailing edge loss [24], which arises due to wake mixing, as an addition to profile loss arising at the trailing edge. Trailing edge loss manifest as the loss of total pressure;
3. Losses due to the heat-transfer to surroundings. These manifest as total energy losses.
4. Losses due to windage in the interspace. These manifest as momentum losses.
5. For stators with exit velocities larger than Mach 1, shock losses arise.
6. Secondary losses are induced by complex vortex systems within a turbomachinery stage [25]. Among a variety of vortices, tip clearance vortices, hub and tip endwall vortices are most instrumental in causing substantial losses, which manifest as total pressure loss.

Among these losses, due to the small dimensions and high flow velocities, the heat transfer loss is typically negligible. The remaining losses can be adequately captured as momentum losses. These affect both the angular momentum and the total pressure and can be appropriately captured by setting the respective loss coefficients η_p and η_q as introduced in Eqs. (17) and (14).

2.5. Finding matching rotor inlet conditions

The methodology described in preceding sections, allows the estimated rotor inlet conditions (p_{4c}, T_{4c}, C_{4Rc}, C_{4Tc}) to be calculated from a set of stator outlet properties (p_3, T_3, X_3, α_{3b}). However, we need to iteratively adjust the value of guessed stator outlet conditions M_3, p_3, and α_{3b} that making the estimated rotor inlet condition (p_{4c}, T_{4c}, C_{4Rc}, C_{4Tc}) equalling to the target rotor inlet conditions. This solving process requires a optimisation-like equation solver.

In this study, we adopt `scipy`'s `root` multivariate root-finding algorithm with the *hybr* method, which uses MINPACK's *hybrd* and *hybrj* routines (modified Powell method) [26] to solve

$$F(X) = 0 \,, \tag{19}$$

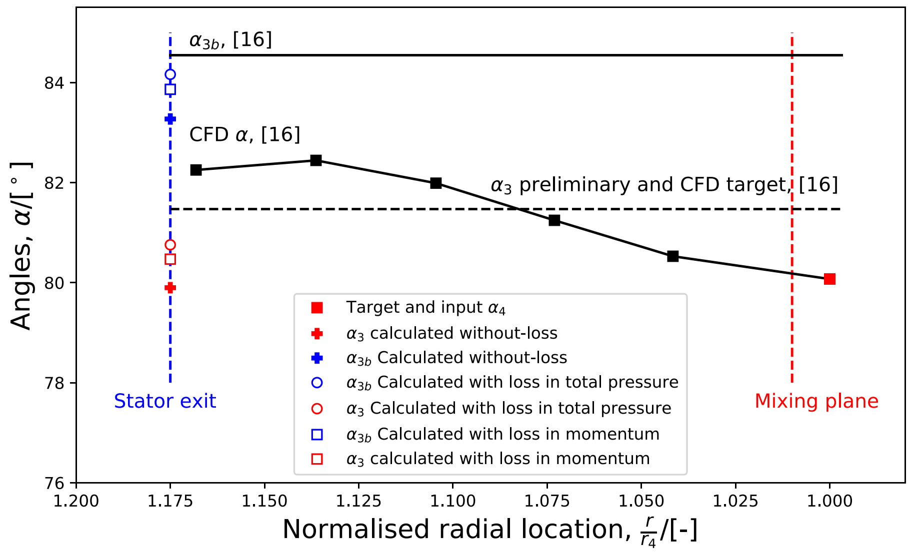

Fig. 5. Variation of absolute flow angle across the stator rotor interspace. Lines showing CFD data are reproduced from [17].

Table 2
Stator and rotor geometry parameters used for verification geometry [17].

r_4/[mm]	$\frac{r_3}{r_4}$	α_{3b}/[°]	Z_s	t_3/[mm]	δ/[°]	Z_r	t_r/[mm]	b_4/[mm]	A_4/[m^2]
60.19	1.175	84.5	21	0.5	3.47	16	0.5	1.85	6.70×10^{-4}

with:

$$F(X) = \begin{cases} f_{p_{4c}}(p_3, T_3, X_3, \alpha_{3b}) & - & p_{4t} \\ f_{T_{4c}}(p_3, T_3, X_3, \alpha_{3b}) & - & T_{4t} \\ f_{C_{4Rc}}(p_3, T_3, X_3, \alpha_{3b}) & - & C_{R4t} \\ f_{C_{4Tc}}(p_3, T_3, X_3, \alpha_{3b}) & - & C_{T4t} \end{cases} \tag{20}$$

Here, fs are the solutions to the equations from the previous section.

2.6. Design space map generation

Design space maps are generated by repeating the solution process for the ranges of Z_s, t_3, r_3 and δ.

3. Verification and setting loss coefficients

To validate the developed approach, the best idea is to compare the obtained result from the developed approach against high-quality experimental data. However, high-quality experimental data, especially data considering the rotor–stator interspace effect, are hardly published in the open literature. Hence, using high-fidelity CFD results to verify this 1D approach is a viable alternative.

In this case, we compare the results and the variation of flow properties across the interspace to numerical (CFD) simulations from the literature [17], as this CFD data are high-fidelity and recognised with a high academic reputation journal. For this, we use the stage design provided and simulated by Keep et al. [17]. Keep et al. [17] report the variation of absolute flow angle (α) as a function for radial location ($\frac{r}{r_4}$) in the stator–rotor interspace for their CFD simulation with radius ratio, $\frac{r_3}{r_4}$ equal to 1.175. Their stator and rotor geometry is generated by using the preliminary design tool TOPGEN [18]. The relevant geometry parameters are shown in Table 2. Table 3 lists the operation conditions corresponding to the nominal design and values extracted from the CFD. Details of the CFD set-up are available in Keep et al. [17].

The variation of absolute flow angle α (flux average), extracted from the CFD simulations with respect to normalised radial distance ($\frac{r}{r_4}$) is recreated in Fig. 5. The *CFD results* show that there is a substantial jump between the blade angle, α_{3b} and the first flow angle recorded in the interspace. This reduction of approximate 2.5° is attributed to two factors. First, due to the deviation at the stator exit, the flow turns inwards. This is counteracted by the sudden expansion that takes place as the flow exits the stators, which turns the flow outwards to achieve a flow angle of approximate 82.1°, as shown in Fig. 5. Thereafter the flow keeps turning inwards as the interspace is crossed. As shown in Fig. 5, the final angle, 80.07° is below the design intend of 81.5°.

The remainder of this section focuses on tuning the loss coefficients, η_p and η_q, to correctly account for the losses seen in the CFD case followed by a comparison of modelled and simulated flow angles.

3.1. Selection of loss coefficients

The first demonstration of the design tool is possible by using the flow conditions of the rotor inlet (location 4) listed in Table 3, *CFD results* and geometry parameters from Table 2 to calculate the corresponding stator blade angle, α_{3b} and corresponding flow angle, α_3. Results of the case without losses (Case 0, $\eta_p = 0$, $\eta_q = 0$) are shown by the crosses in Fig. 5. Here, the blade angle, α_{3b} is underpredicted by approximate 1°.

Results of Cases 1a and 2a, corresponding to η_p and η_q of 10.15%, are shown by the open circles and squares in Fig. 5 and the actual data are summarised in Table 4. The value of 10.15% is chosen, as it matches the losses from CFD simulations stated by Keep et al. [17]. These cases result in a closer agreement between the calculated and actual blade angles.

Case 1b and Case 2b have increased total pressure and momentum losses so that a blade angle $\alpha_{3b} = 84.50°$ is achieved. Considering these, the stator exit pressure in Case 1b is above the supplied pressure, while that in Case 2b is much lower than the supplied pressure. To exactly match the stator exit conditions, Case 3 uses iteratively obtained values for the two loss coefficients so that α_{3b} matches total conditions, and the values are $\eta_q = 10.15\%$ and $\eta_p = 6.65\%$. The loss coefficients from Case 3 are used for simulations *with losses* in the remainder of this paper.

The losses listed in Table 4 can be compared to the entropy losses reported in the CFD study by Keep [17]. The entropy loss upstream of the rotor converts to a total pressure loss of approximately 10.15%

Table 3
Flow states, design intend and results from CFD [17].

Parameter	p_{01}/[Pa]	T_{01}/[K]	N/[RPM]	α_4/[°]	C_4/M_4	p_4/[Pa]	T_4/[K]
Intend	2×10^7	833	50×10^3	81.5	324.80/0.747	1.323×10^7	779.1
CFD results	2×10^7	833	50×10^3	80.07	319.95/0.720	1.348×10^7	782.7

Table 4
Comparison of stator exit conditions for different loss model configurations.

Model	η_p/[%]	η_q/[%]	α_3/[°]	α_{3b}/[°]	p_{03}/[MPa]	T_{03}/[K]
Actual geometry	n/a	n/a	n/a	84.50	< 20.0	833.0
Case 0	0	0	79.90	83.27	**17.97**	833.0
Case 1a	10.15	0	80.76	84.16	**19.99**	833.0
Case 1b	14.22	0	81.08	**84.50**	20.94	833.0
Case 2a	0	10.15	80.47	83.86	**17.97**	833.0
Case 2b	0	22.06	81.08	**84.50**	**17.97**	833.0
Case 3	10.15	6.65	81.08	**84.50**	**19.99**	833.0

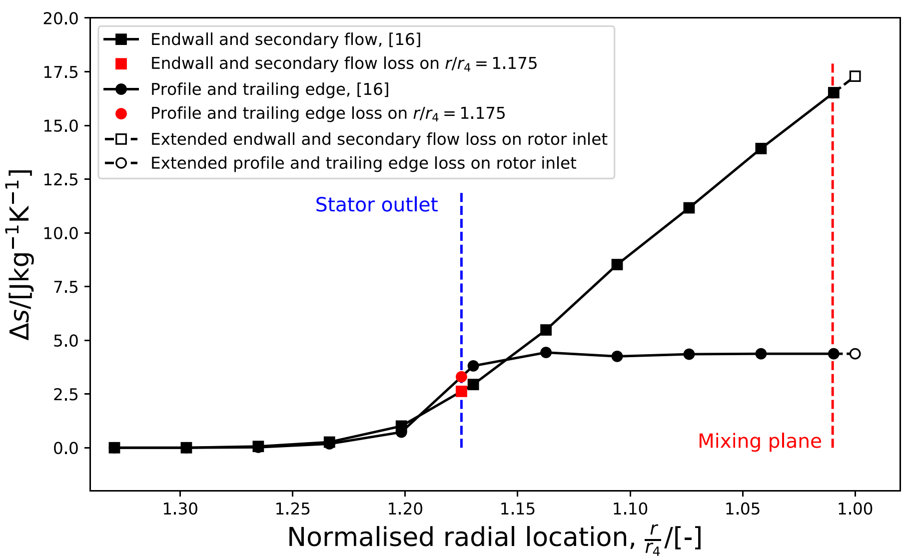

Fig. 6. Entropy rise across the stator–rotor interspace, reproduced from Keep et al. [17].

(calculated from entropy rise shown in Fig. 7 of [17], as outlined in Appendix B). Case 1b and Case 2b, whose blade angles match the actual geometry well, have different mismatches in the loss coefficients. Even though Case 1b returns the minimum mismatches in loss, its total pressure exceeds the requirement of the total conditions. Case 2b returns the lowest total conditions, however, the loss percentage is the largest, with η_q of 22.06%.

Hence, to tune the loss coefficient, Case 3 is presented. To achieve the correct flow, we need to apply a total pressure loss of 10.15%, which matches the desired entropy loss. In addition, we need to apply a 6.65% angular loss, which indicates that most of these losses are incurred due to friction in the tangential direction and that we are using η_q to account for the flow angle.

3.2. Comparison of flow angles between analytical model and CFD

To provide further insight on the flow in the interspace, the analytically determined flow angles for Case 3 in the stator–rotor interspace are compared to the *CFD results* from [17]. As the tuned loss coefficients are used, the flow at the boundaries (α_4 and α_{3b}) agree. When calculating the flow angles at the intermediary points, it is assumed that the losses increase as one crosses the interspace. We investigate two loss variations in this study:

- As shown in Fig. 6, different types of losses (endwall, secondary flow, profile and trailing edge losses) are generated in the interspace. However, all of these losses can be put down to total pressure loss, η_p. The amount of entropy rise follows different trends of the normalised locations of $\frac{r}{r_4}$, and the η_p can be calculated as a function of radial locations through the methodologies listed in Appendix B. Hence, by using Fig. 6, the $\eta_p = f(\frac{r}{r_4})$ can be obtained. The η_q is set to zero in this case.
- The losses which linearly increase with radial location are calculated through:

$$\eta_{j,total} = \frac{\frac{r}{r_4} - 1.175}{1.0 - 1.175}\,\eta_j \,, \tag{21}$$

where j can be p or q, indicating total pressure loss or momentum loss. In this section, we use the tuned loss coefficient of Case 3, i.e. $\eta_p = 10.15\%$ and $\eta_q = 6.65\%$.

With the function of η_j, forward calculation (to solve the control equations across the stator–rotor interspace) is carried out for different radial locations $\frac{r}{r_4}$. A special case is applied for $\frac{r}{r_4} = 1.175$, i.e. at the stator outlet. Here, the flow area is set to equal to the stator outlet flow area. Thereafter, the flow area is $A = 2\pi r$, to simulate the cylindrical flow surface inside the stator–rotor interspace. Finally, for $\frac{r}{r_4}$ equal to 1.0, the rotor leading edge thickness is set to 0.5 mm, to simulate the actual rotor inlet condition. The results are displayed in Fig. 7.

As shown in Fig. 7, there is a qualitatively good agreement between the analytical and CFD solutions for both approaches. For both approaches, there is a large increase of α directly after the stator outlet section. The first points for the analytical model correspond to the flow

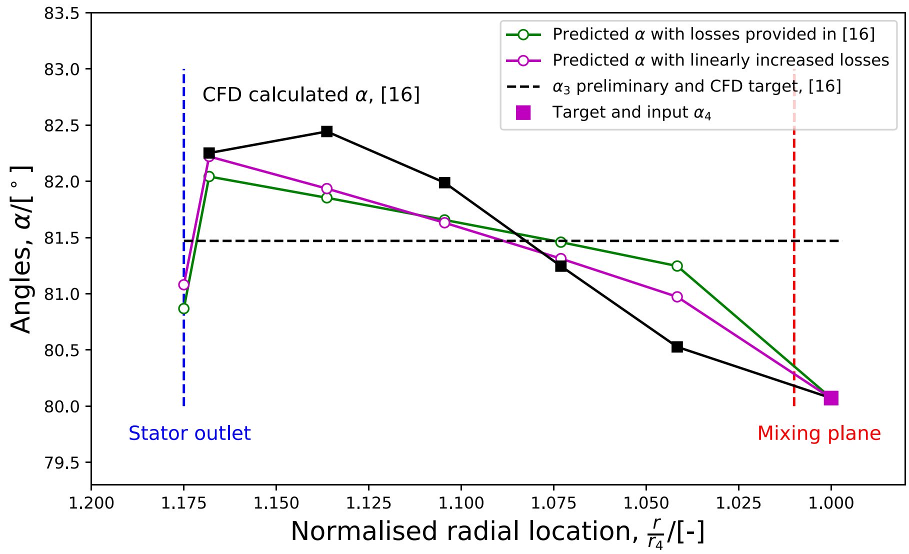

Fig. 7. Comparison of flow angles between CFD [17] and analytical model corresponding to Case 3 from Table 4.

that has turned to α_3 in the stator passage, but before exiting the stator. The subsequent increase in flow angle arises due to the increase in the effective flow area at the stator exit.

For approach 1, by using the losses gained from the study [17], the predicted α through our approach is 82.04°, while the value predicted by CFD is 82.25°, with a difference of 0.21°, 0.25%. For approach 2, using the losses that linearly increase, the predicted α through our approach is 82.22°, which is almost coincident with *CFD results*. These indicate that both approaches have good agreement with *CFD results*. Both approaches accurately capture the increase of angles at stator exit, i.e. jumping from ~81.0° to ~82.25°.

Then in the stator–rotor interspace, the predicted α of both approaches show a gradual decrease, which has the same trend as the predicted α of CFD. There is a mismatch in slope between the values predicted by CFD and analytically predicted angles. Early in the outer part, i.e. in the area between $\frac{r}{r_4}$ = 1.15 and 1.10, the flow, in reality, is more tangential. If the data from Table 4 are considered, losses will make the flow turn inwards. Hence, for the outer part of the interspace, losses, in reality, are probably smaller than those assumed by the analytical model. Following on, in the inner part of the interspace, the flow is more vertical. Hence, the losses here are lower than the values predicted by the analytical model.

These results show that the developed model captures the key features affecting flow angle. This gives us confidence in the capabilities of the modelling approach and the results presented in the following sections.

4. Results and discussion

To assist with the future designs of RITs, the developed approach is employed to evaluate the stator design space for a 500 kW sCO_2 turbine design. The rotor inlet geometries and desired flow properties are obtained using the in-house preliminary design code TOPGEN [1,18], listed in Table 5.

Table 6 shows the input parameter ranges used for the stator design exploration. The range for $\frac{r_3}{r_4}$ (i.e. 1.02, 1.05 and 1.08) is set based on a study conducted by Keep et al. [17]. The study [17] has shown that end-wall losses increase for $\frac{r_3}{r_4}$ above 1.05, while the trailing edge loss and entropy increase because stator–rotor interaction becomes significant as $\frac{r_3}{r_4}$ approaches 1.02. A 1.08 case is added to give an expansion for the research space. For small-scale RITs, the stator blade number Z_s can be calculated through Eq. (C.2), which is listed in Appendix C. Considering the power scale of 500 kW, a range of 12 to 26 covers the most possibilities [1]. Considering the machining limit of the trailing edge thickness of 0.9 mm, a range of 0.5 mm to 1.5 mm will be used in this study.

Table 5
Design parameters for the 500 kW sCO_2 RIT rotor.

Parameters	Value
Power [kW]	500.00
Rotational speed N [kRPM]	100.0
Inlet radius r_4 [mm]	31.63
Inlet static temperature T_4 [K]	790.40
Inlet static pressure p_4 [MPa]	14.70
Inlet absolute velocity C_4 [m s^{-1}]	311.42
Inlet Mach number M_4 [–]	7.08×10^{-1}
Rotor blade number Z_r [–]	13
Rotor blade thickness t_r [mm]	1.0
Inlet area A_4 [m^2]	6.02×10^{-4}
Inlet blade height b_4 [mm]	2.38
Inlet flow absolute angle α_4 [°]	66.16

Table 6
Input value for the stator calculation.

Parameters	Value
Radius ratio r_3/r_4 [–]	1.02, 1.05, 1.08
Stator blade number [–]	12 to 26
Trailing edge thickness [mm]	0.5 to 1.5
Total pressure loss ratio η_p	10.15%
Momentum loss ratio η_q	6.65%

4.1. Stator geometry calculated, assuming no losses

To give a good understanding of the design space for the stator NGVs, the results from each design space exploration are shown as contour maps of stator trailing edge thickness t_3 and stator blade angle α_{3b}, with three maps generated corresponding to the interspace ratios. Each design map includes 165 potential stator geometrical designs, with different combinations of design parameters. In these figures (e.g. Fig. 8), the black dashed lines, corresponding to contours of stator blade number, Z_s, show the required blade angle, α_{3b}, which is required for different trailing edge thickness, t_3. The blue dashed line illustrates the empirical lower limit for the trailing edge thickness, t_3, discussed in the following section.

The results in Fig. 8 show that outlet Mach number, M_3, increases with the increased trailing edge thickness of t_3, which is caused by

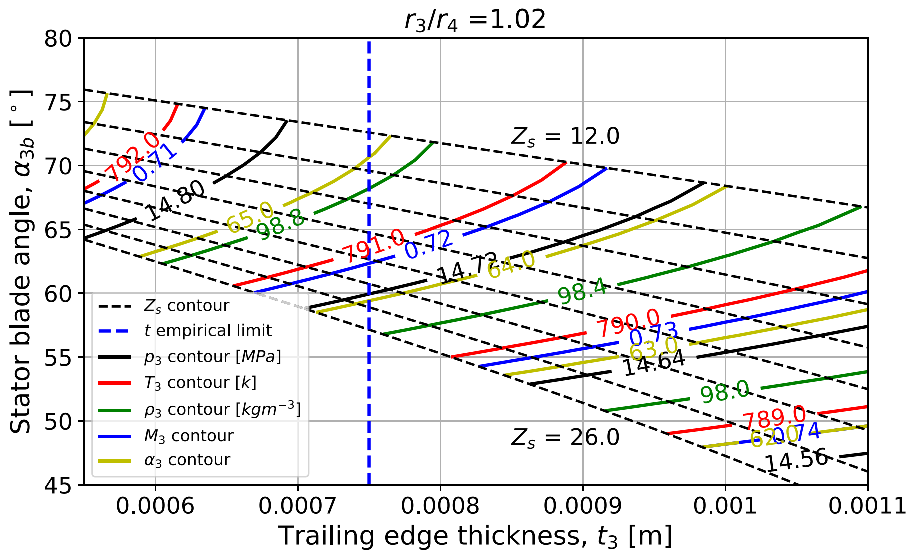

Fig. 8. The design spaces for the stator NGVs at radius ratio of 1.02.

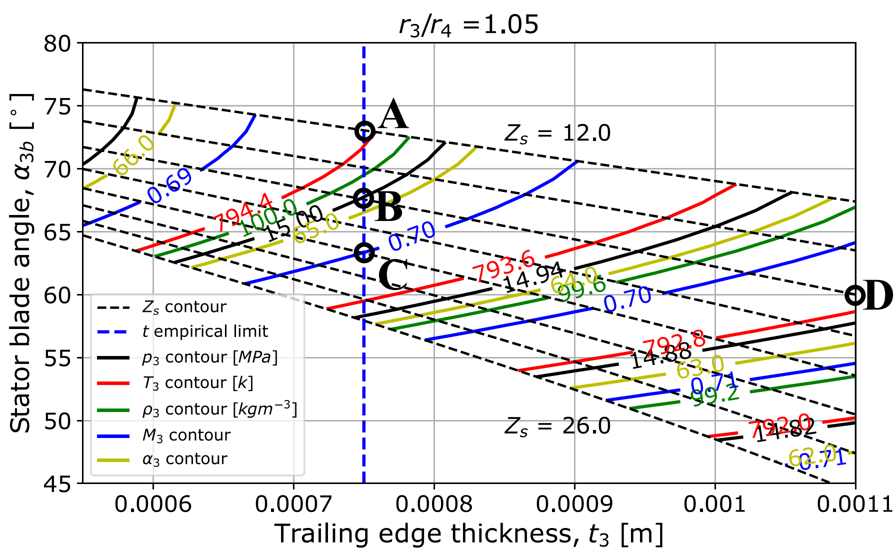

Fig. 9. The design spaces for the stator NGVs at radius ratio of 1.05.

the reduction in effective flow area as trailing edge thickness t_3 increases. Simultaneously, as Mach number increases, the blade angle α_{3b} decreases to ensure the desired tangential velocity is maintained. Similarly, the outlet flow angle α_3 is reduced with the increased trailing edge thickness, t_3.

As trailing edge thickness increases, p_3, T_3 and ρ_3 decrease, which makes sure the balance of the energy equation.

However, if the design space with different NGVs blade number Z_s is emphasised, it can be found that the outlet blade angle α_{3b} decreases with increased Z_s. The influence of Z_s reduces as Z_s increases, i.e. the value of $\frac{\Delta\alpha_{3b}}{\Delta Z_s}$ reduces. At the same time, the outlet Mach number M_3 increases, while α_3 decreases. Similarly, p_3, T_3 and ρ_3 also decrease with increased Z_s.

Figs. 9 and 10 shows the design spaces of M_3, α_3, p_3, T_3 and ρ_3 at the radius ratios $\frac{r_3}{r_4}$ of 1.05 and 1.08 respectively, providing insight on the impact of changes in $\frac{r_3}{r_4}$. It can be seen that as the $\frac{r_3}{r_4}$ increased, the whole design space moves slightly upward and towards larger α_{3b}. M_3 shows an opposite behaviour, which is a reduction with increased $\frac{r_3}{r_4}$ values. This is an expected trend, caused by an increase in available flow area with r_3, which reduces nozzle exit Mach number, and the need to maintain angular momentum. The static outlet pressure p_3, the static outlet temperature T_3 and the outlet flow density ρ_3 increases with increased $\frac{r_3}{r_4}$.

4.2. Comparison of near optimal designs

We now select 4 specific geometries to explore the designs in detail. These designs are selected by identifying the preferential region of the design space.

First, the outlet Mach number should be minimised, to reduce the trailing edge losses due to potential shocks and viscous effects. Thus, the designs close to the top left are preferred. Second, the work by Keep et al. [17], studying low specific speed turbines has shown that the radius ratios of 1.05 are favourable (smaller ones, e.g. $\frac{r_3}{r_4}$ = 1.02, experience high losses due to trailing edge losses and mixing and stator–rotor interaction; larger ones, undergo the increase in end-wall losses). Because of this, we select $\frac{r_3}{r_4}$ = 1.05 for further analysis. Then, as shown in Fig. 9, the blue dashed line illustrates the empirical limit for the trailing edge thickness, t_3. Even though a thin trailing edge leads to uniform outflow and less trailing edge loss, due to the machining limit, a typical limit for trailing edge thickness is 0.9 mm [1].

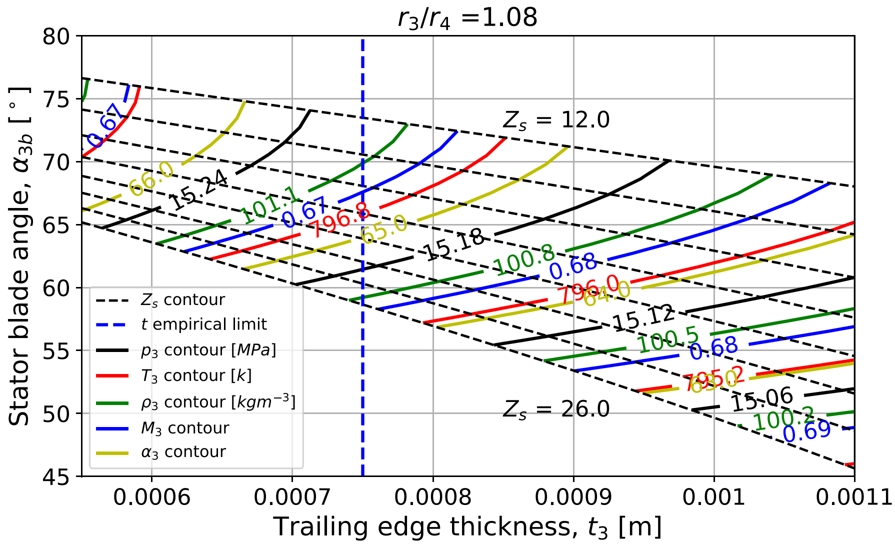

Fig. 10. The design spaces for the stator NGVs at radius ratio of 1.08.

Table 7
Design parameters for stator NGVs.

Parameters	Case **A**	Case **B**	Case **C**	Case **D**
Radius ratio r_3/r_4 [–]	1.05	1.05	1.05	1.05
Outlet radius r_3 [mm]	33.21	33.21	33.21	33.21
Stator blade number Z_s [–]	**12**	**16**	**22**	**16**
trailing edge thickness t_3 [mm]	0.9	0.9	0.9	1.5
Outlet blade angle α_{3b} [°]	73.05	67.56	61.41	61.12
Inlet flow angle α_1 [°]	49.77	49.62	49.30	48.81
Outlet flow angle α_3 [°]	65.35	65.08	64.49	63.62
Outlet Mach number M_3 [–]	0.692	0.694	0.697	0.703
Outlet static pressure p_3 [MPa]	15.01	15.00	14.96	14.91
Outlet static temperature T_3 [K]	794.43	794.22	793.78	793.09
Outlet flow density ρ_3 [kg m^{-3}]	100.04	99.96	99.78	99.50
Total throat width, A_3/b_3 [m]	0.185	0.183	0.178	0.172
Outlet absolute velocity C_3 [m s^{-1}]	298.48	299.13	300.60	302.82
Outlet radial velocity C_{3R} [m s^{-1}]	124.47	126.03	129.47	134.56
Outlet tangential velocity C_{3T} [m s^{-1}]	271.29	271.29	271.29	271.29

Based on the above discussion, 4 cases have been selected on the map that is labelled with **A** to **D** in Fig. 9. **A**, **B**, **C** have been selected to fall on the minimum thickness line and **D** further to the right of the lower Mach number region. By comparing **A**, **B** and **C**, the effect of changing Z_s can be revealed. Similarly, by comparing **B** and **D**, the effect of changing t_3 can be illustrated. Details about the design parameters are shown in Table 7.

It is significant to choose a good Z_s to minimise the losses and enhance the performance of the stator. It can be seen in Table 7 that the inlet flow angle α_1 decreases with the increase of Z_s. At the outlet section, that C_3 and C_{3R} increase with increased Z_s, while A_3/b_3 reduces with increased Z_s, so as to keep the continuity balance. Small Z_s may potentially reduce the friction loss, as the blade surface area are reduced. However, a large flow area may reduce the uniformity of the outlet flow, as small Z_s reduce the guidance of the flow direction. In the opposite way, large Z_s may reduce the throat area, potentially increasing the outlet flow Mach number. The losses increase with M_3 and increasing hydraulic ("wetted", or contacted blade) surface area, hence as for reducing the loss in the stator, lower Z_s cases are preferred.

To have a better view of the designed blade geometries, schematics for the 4 design cases are shown in Fig. 11. As shown in Fig. 11, the dashed blue line shows the position of the L_T, which illustrates the throat area. The fluid inside the blade channel first accelerates and then expands after the throat section. Fig. 11(a) shows that the end of L_T is located in the upper stream of the NGV pressure side, which means once the working fluid enters into the blade channel, only expansion happens, that the NGVs have limited guidance on the inlet flows. In this case, $Z_s = 12$ is not within our interest.

Comparing Fig. 11(b) and Fig. 11(d), i.e. the Case **B** and the Case **D**, it is obvious that the outlet Mach number increases with added outlet blade thickness t_3, therefore, losses are increased. With the above discussion, the Case **B** is better, and is recommended as a favourable design case.

4.3. The effect of losses on the stator shape and exit conditions

A study [17] has recommended the radius ratio $\frac{r_3}{r_4} = 1.05$, because the interspace losses are the smallest. In this section, a radius ratio $\frac{r_3}{r_4} = 1.05$ is used to investigate how losses generated in the interspace affect the flow, and the geometrical and operational properties of the stator NGVs. In this study, we use Case 3 from Section 3.1 with loss coefficients $\eta_p = 10.15\%$ and $\eta_q = 6.65\%$ as this arrangement yields the best agreement between CFD and our analytical model. Similar to the previous section, the design spaces for a trailing edge thickness t_3 from 0.5 mm to 1.5 mm and stator blade number from 12 to 26 are shown in Fig. 12.

Comparing Figs. 12 to 9, the corresponding one without losses, it is observed that M_3 increases for the whole design space. This is due to the momentum losses, which require increased total pressure and velocity at the stator outlet. The outlet flow angle α_3 also increases, compared to the designs without losses. It is also observed that both p_3 and ρ_3 also increase, while T_3 decreases compared to the designs

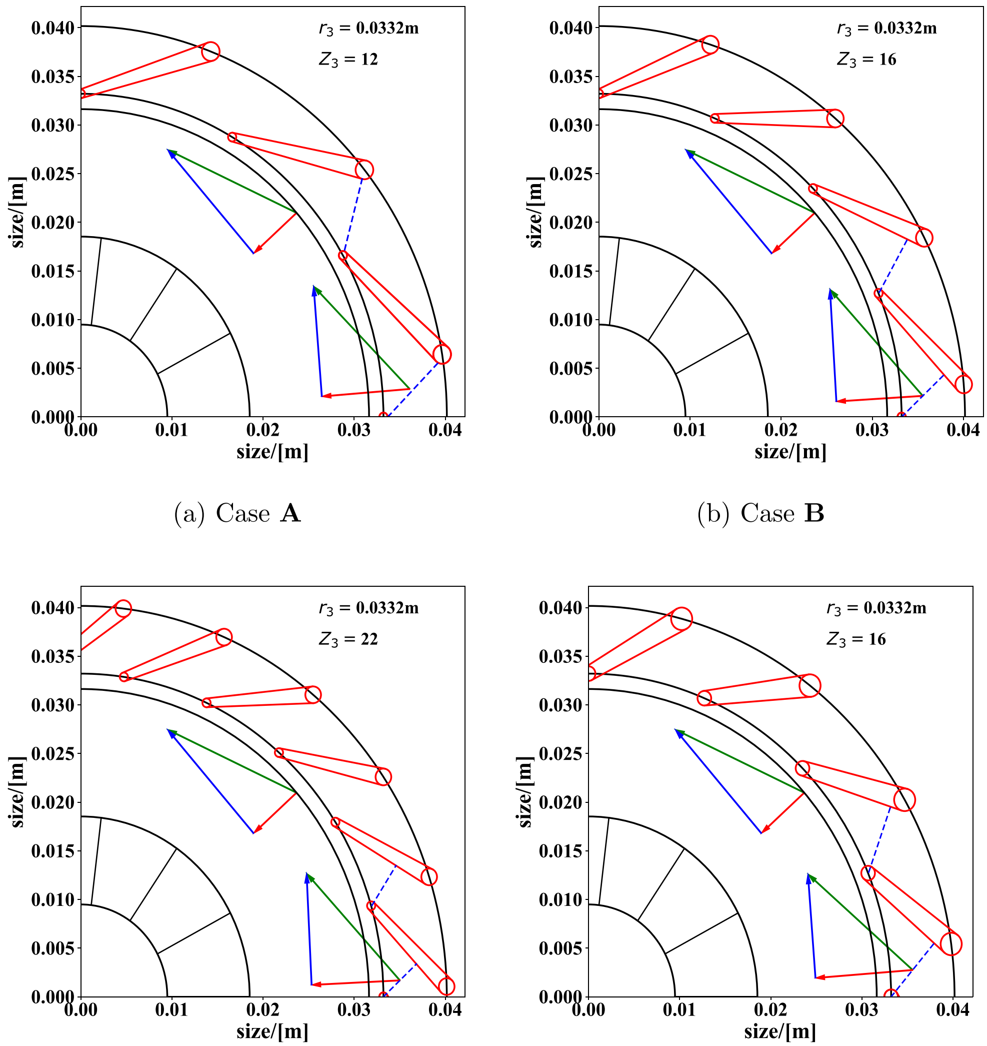

(a) Case **A** (b) Case **B**

(c) Case **C** (d) Case **D**

Fig. 11. Plots showing stator NGVs geometry for $\frac{1}{4}$ of turbine. The velocity vectors for stator outlet flow and rotor inlet flow are plotted on the figure. Green — absolute flow velocity, red — the radial components, blue — the tangential components, dashed blue — L_t.

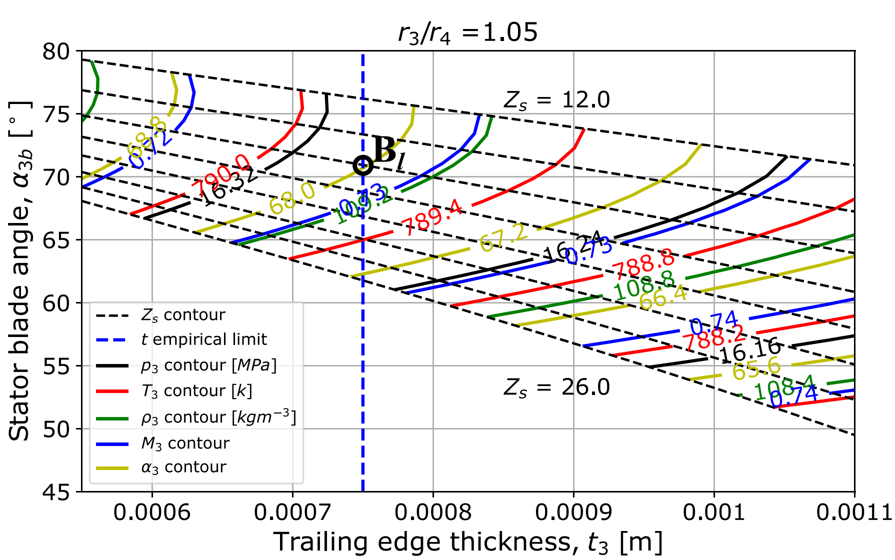

Fig. 12. The design space for the stator NGVs at radius ratio of 1.05, with loss coefficients of η_p = 10.15% and η_q = 6.65%.

Table 8
Design parameters for stator NGVs.

Parameters	Case ***B***	Case ***B$_l$***
Radius ratio r_3/r_4 [–]	1.05	1.05
Outlet radius r_3 [mm]	33.21	33.21
Stator blade number Z_s [–]	16	16
trailing edge thickness t_3 [mm]	0.9	0.9
Outlet blade angle α_{3b} [°]	**67.56**	**70.92**
Outlet flow angle α_3 [°]	**65.08**	**68.01**
Outlet Mach number M_3 [–]	**0.694**	**0.729**
Outlet static pressure p_3 [MPa]	**15.00**	**16.30**
Outlet static temperature T_3 [K]	**794.22**	**789.76**
Outlet flow density ρ_3 [kg m^{-3}]	**99.96**	**109.28**
Total throat width A_3/b_3	**0.183**	**0.179**
C_3 [m s^{-1}]	**299.13**	**313.40**
C_{3R} [m s^{-1}]	**126.03**	**117.32**
C_{3T} [m s^{-1}]	**271.29**	**290.61**
Outlet total pressure p_{03} [MPa]	**19.47**	**21.67**
Inlet total pressure p_{04} [MPa]	19.47	21.67
Outlet total temperature T_{03} [MPa]	839.94	839.94
Inlet total temperature T_{04} [MPa]	839.94	839.94

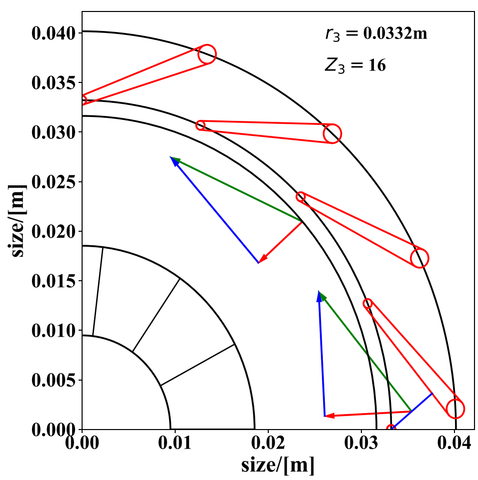

Fig. 13. Plot showing stator NGVs geometry for $\frac{1}{4}$ of turbine corresponded to the case with interspace loss.

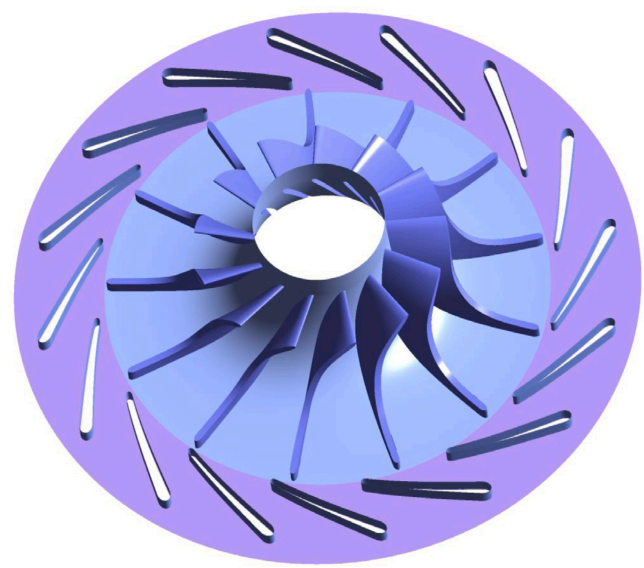

Fig. 14. 3D geometric model of the sCO_2 radial turbine.

without losses. These changes are required to compensate for the total pressure and angular momentum losses, while balancing the energy and continuity equation.

To provide a more direct comparison, Case **B**$_l$, corresponding to Case **B** in Fig. 9, is selected and the two cases are compared in Table 8. The most pronounced changes are the increase in total pressure, p_{03}, and the increase in stator exit blade angle, α_{3b}, of 2.2 MPa and 3.36°, which are required to compensate for the losses in total pressure and angular momentum that exist in the stator to rotor interspace. Fig. 13 shows the corresponding velocity triangles at the stator exit and rotor inlet.

As shown in Table 8, for the turbine sizes considered in the current study, it is important to appropriately account for the losses in the interspace, so as to maintain the desired rotor inflow conditions. For example, for turbine scale analysed here (sCO_2 turbine with power outputs of the order 500 kW), an adjustment of 3.36° and 2.2 MPa to the stator exit angle and total pressure are required. This illustrates the importance of considering interspace losses when designing a stator to suit a given rotor and carrying out the preliminary design of rotors.

Both Keep [17] and Wheeler [21] have studied the losses of stators in isolation and their studies have shown that these losses can have a notable impact on overall performance. In the current work, we provide further insight on how these losses influence the flow conditions that can be attained at the rotor inlet and on the adjustments of inlet conditions and stator geometry required to attain the desired rotor inflow conditions. Without appropriately considering the interspace losses, the desired rotor inlet conditions will not be reached. Hence, including the stator losses in turbine design, especially in small-scale sCO_2 turbines, is very significant.

4.4. Verification through three-dimensional CFD simulations

It is necessary to conduct the experimental verification to ensure the rationality of the design data and the selected total pressure and momentum losses in the paper. However, the three-dimensional (3D) CFD numerical simulation becomes the optimal choice due to the limited experimental conditions. The structural parameters of the rotor are obtained from `TOPGEN` and the design conditions are shown in Table 5. The structural data of the stator are chosen from the values listed in Case **B**$_l$, with $\delta = 2°$ and the stator blade length of 15 mm. Based on the ANSYS platform, the simulation adopts the `BladeGen` module to model the RIT, and the model of the rotor is shown in Fig. 14. Besides, a fully structured grid is generated by adopting the `TurboGrid` module. The wall distance is directly related to the dimensionless wall distance, y$^+$, which is defined by the turbulence model. For the SST k-ω model, it uses an automatic wall function, the near wall element y$^+$ value should be within the log-law region, in the range of 30 to 300. Keeping the y$^+$

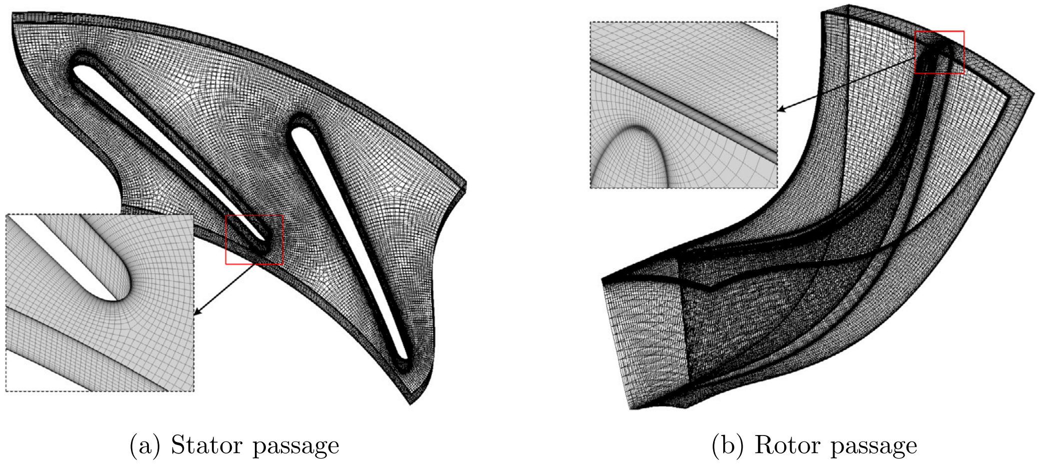

Fig. 15. Computational grid of the turbine passages.

Table 9
Grid independence study.

Group	Rotor/[$\times 10^3$]	Stator/[$\times 10^3$]	Power/[kW]	η_{ts}/[%]	M(all blades)/[Nm]
1	405	155	502.70	78.31	48.12
2	625	200	501.26	78.46	47.98
3	950	310	499.10	78.48	47.77
4	1376	446	499.45	78.41	47.81

in this range should capture the most important flow behaviour with acceptable mesh resolution and short simulation time. In this paper, the y^+ range is 2.1 to 124.2 for the stator, with the average value is 70.9; the y^+ of the rotor is in the range of 4 to 100.9, with an average value of 49.1.

Since different grid numbers affect the accuracy of simulation and the dense grid wastes computing time and resources, this paper employs four meshes with different resolutions to verify the grid independence. Then, the effect of the number of cells on the simulated results is confirmed by the variation of Power, Isentropic efficiency (η_{ts}) and Torque (M), so as to finally determine the appropriate mesh, with the validation results shown in Table 9. In this study, the No. 3 mesh (with 2 stators, 1 rotor passage, in total 1570×10^3 cells) is finally selected to conduct the numerical simulation and result analysis, as shown in Fig. 15. To introduce the real gas properties of the CO_2, the physical parameters are provided by the open-source database CoolProp [27]. Its physical properties are calculated on the basis of the Span and Wagner EoS. This EoS is the fundamental equation expressed in the form of Helmholtz energy [28], as follows,

$$A(\rho, T)/(RT) = \phi(\delta, \tau) = \phi^o(\delta, \tau) + \phi^r(\delta, \tau) \ . \tag{22}$$

where $\delta_1 = \rho/\rho_c$, $\tau = T_c/T$, $\rho_c = 467.6$ kg m^{-3} and $T_c = 304.1282$ K. $\phi^o(\delta, \tau)$ is the formula describing the ideal-gas of the Helmholtz energy, and $\phi^r(\delta, \tau)$ is used to describe the residual part of the Helmholtz energy.

The in-house Python program is utilised to generate the Real Gas Properties (RGP) table which will be used for transferring the gas properties to CFX. The RGP table must have a wider data range, that the pressure range of 8 MPa to 24 MPa and the temperature range of 400 K to 900 K, to cover the operating conditions. At the same time, the resolution of the table affects the simulation results [29], so it is pivotal to choose a table with an appropriate resolution. After conducting the irrelevance verification of the table resolution, a table with a resolution of 400 × 400 is finally selected for simulations.

In this paper, the ANSYS CFX software [30] based on the 3D Navier–Stokes equation is adopted to conduct the numerical simulation. As the developed approach reflects the steady-state operational conditions within the stator and stator–rotor interspace, it can hardly provide loss variations with time. Hence, in this study, steady-state CFD simulations are carried out.

According to the Case $\boldsymbol{B}_l$, the total pressure at stator inlet is 22.1 MPa and the total temperature is 840 K, and the $\dot{m}$ at the rotor outlet is 5.69 kg s^{-1}. The $k-\omega$ SST model is adopted as the turbulence model because its prediction about the flow under adverse pressure gradient (like separated flow) is more accurate. The staging method (Mixing-Plane) is selected to exchange information between dynamic and static domains. A no-slip wall boundary condition is applied for the solid wall. The residual value of the convergence limit of each physical quantity is set as 10^{-5}. Finally, the results obtained from the 3D numerical simulation are compared with the data from the one-dimensional(1D) result. On the one hand, the power output of the turbine and the outlet parameters of the stator are analysed, as shown in Table 10, indicating that the output power of the turbine is consistent with the design. Besides, the exit velocity triangle of the stator obtained from the 3D simulation basically accords with the data from the 1D design, and the outlet Mach number of the stator meets the design requirements. On the other hand, the inlet conditions of the rotor (including the velocity triangle of the rotor inlet and M_4) are analysed, with the comparison results shown in Table 11, indicating that the relative errors are acceptable. In short, the 3D simulation results are consistent with the 1D design results, and the relative errors of all values are within 5%, which fully demonstrates the rationality of the workflow in this paper.

To present the rationality of the 3D simulation process more clearly, Fig. 16 shows the streamlines of the blade lattice passage of the turbine. Firstly, CO_2 accelerates in the nozzle and reaches the maximum speed at the nozzle throat, and then continues to expand inside the rotor. It can be observed that the streamline distribution follows the design process and most of the streamlines in the rotor follow the flow path distribution, indicating that the designed turbine geometry matches the operation parameters. Fig. 17 is the static pressure contours of the turbine at different spans. The static pressure decreases smoothly to about 10 MPa along the stage passage. The pressure drop rate gradually decreases in the rotor and the pressure face always maintains a higher static pressure than that in the suction surface, which manifests that the profile of the rotor blades is designed well to ensure the strong operation capacity of the rotor.

Table 10
Turbine power and stator outlet data.

Case	Power/[%]	α_3/[°]	C_3/[m s^{-1}]	C_{3R}/[m s^{-1}]	C_{3T}/[m s^{-1}]	M_3/[–]
1D results	500.0	68.01	313.40	117.32	290.61	0.729
3D CFD results	499.1	68.00	319.07	118.26	294.75	0.722
relative error/[%]	0.2	0.1	1.8	0.8	1.4	1.0

Table 11
Rotor inlet velocity triangle and Mach number.

Case	C_4/[m s^{-1}]	U_4/[m s^{-1}]	W_4/[m s^{-1}]	M_4/[–]	α_4/[°]
1D results	311.42	331.42	134.13	0.708	66.16
3D CFD results	317.67	335.10	128.22	0.718	67.76
relative error/[%]	2.0	1.1	4.4	1.4	2.4

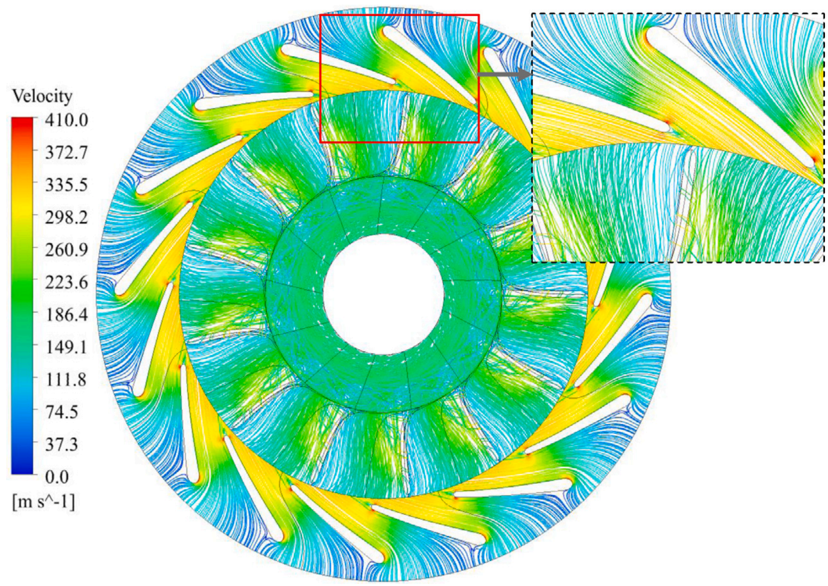

Fig. 16. Streamlines of the 500 kW turbine.

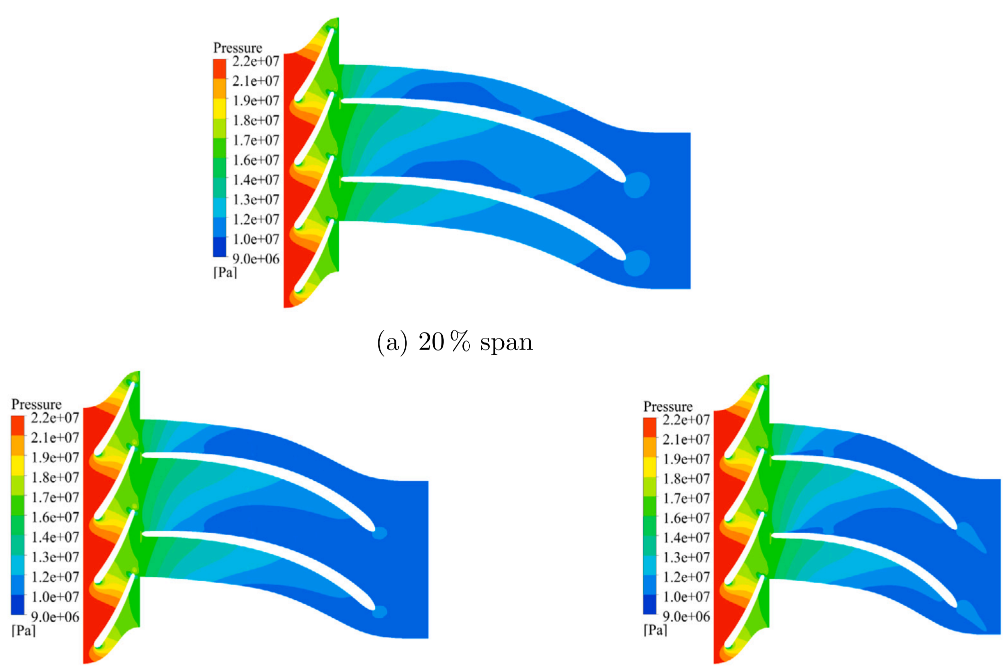

(a) 20 % span

(b) 50 % span

(c) 80 % span

Fig. 17. Static pressure contours of the turbine at different spans.

5. Conclusions

In this study, an analytical workflow connecting RIT stator NGVs outlet geometrical and flow conditions to the rotor inlet conditions has been developed. Through comparison to CFD simulations of a sCO_2 RIT with inlet total conditions of 20 MPa and 833 K and the pressure ratio of 2.22, the empirical total pressure loss and angular momentum loss coefficients are found to be 10.15% and 6.65%.

Next, the analytical model is adopted to develop design space maps to suit the candidate 500 kW sCO_2 RIT. These maps explore how the stator flow conditions and stator exit blade angle to be adjusted, for a range of constraints defined by interspace sizes ($\frac{r_3}{r_4}$ = 1.02, 1.05, and 1.08), blade numbers (Z_s from 12 to 26), and trailing edge thicknesses (t_3 from 0.5 to 1.5). By considering the same constraints without and with losses, the impact of total pressure and angular momentum loss is investigated. Finally, the geometric data of the design is verified by 3D numerical simulation, and satisfactory results are obtained.

The following major findings can be reported:

1. An workflow is developed to accurately model the flow through the stator to rotor interspace;
2. Qualitative analysis of the generated design maps indicates that a stator with $Z_s = 16$, $r_3 = 33.21$ mm and $t = 0.9$ mm, is the preferred design for the 500 kW RIT, due to the potential for reduced losses;
3. By selecting appropriate total pressure and momentum losses, the flow turning within the interspace can be appropriately captured. For the small sCO_2 RITs considered in this study, the appropriate loss coefficients are 10.15% and 6.65% respectively;
4. Significant adjustments to the stator exit geometry (3.36° increase in blade angle) and stator exit total pressure (2.2 MPa increase in total pressure) are required to compensate for the losses;
5. The 3D simulation results obtained by ANSYS CFX are consistent with the 1D design results, which can fully prove the rationality of the workflow.

Together these findings highlight the importance of including the interspace losses when designing the stator to suit a given RIT rotor and during preliminary stage design so that these losses can be appropriately accounted for. Further work should investigate mechanisms to reduce these losses and also explore the scalability of the loss coefficients identified from the current small-scale sCO_2 turbine.

CRediT authorship contribution statement

Jianhui Qi: Conceptualization, Methodology, Software, Validation, Investigation, Writing – original draft. **Yueming Yang:** Software, Validation, Writing – original draft. **Kuihua Han:** Writing – review & editing. **Ming Gao:** Writing – review & editing. **Yingjie Li:** Writing – review & editing. **Suoying He:** Writing – review & editing. **Jinliang Xu:** Project administration, Writing – review & editing, Resources.

Declaration of competing interest

The authors declare that they have no known competing financial interests or personal relationships that could have appeared to influence the work reported in this paper.

Data availability

No data was used for the research described in the article.

Acknowledgements

The authors would like to thank the project supported by Beijing Natural Science Foundation, China (3222048), National Natural Science Foundation of China (Grant No.: 52106049), Natural Science Foundation of Shandong Province, China (ZR2020QE191), Natural Science Foundation of Jiangsu Province, China (BK20210113), National Natural Science Foundation of China (Grant No.: 52130608), and China Postdoctoral Science Foundation (2021M701183), for their financial supports. Vielen Dank an *Dr. Ingo H. J. Jahn* für die Hilfe und Unterstützung meiner Doktorarbeit. Thanks go to *Dr. Kunli Wang* for the milk teas and Lakeside coffees in Brisbane.

Appendix A. Equation of state calls

Solving of the conservation equations relating conditions at stator outlet, station (3) and rotor inlet, station (4), required suitable equations of state. So far these have been described using the generic functions $\boldsymbol{f}_h(p,T)$, $\boldsymbol{f}_\rho(p,T)$, and $\boldsymbol{f}_a(p,T)$, to recover enthalpy, density, and speed out sound respectively. Depending on gas model the following equations may be substituted

For ideal gas, here the functions become:

$$\boldsymbol{f}_h(p,T) = C_p T \ , \tag{A.1}$$

$$\boldsymbol{f}_\rho(p,T) = \frac{p}{RT} \ , \tag{A.2}$$

$$\boldsymbol{f}_a(p,T) = \sqrt{\gamma RT} \ . \tag{A.3}$$

For non-ideal gas, the three functions are replaces by functions call or calls to appropriate property databases (e.g. CoolProp [27]) to recover enthalpy, density, and speed of sound based on current thermodynamic state.

Also the equations for solving stator flow properties are presented here, and for ideal gas, the equations are:

$$T_3 = h_{3t}/(C_p + \frac{1}{2} \cdot M_3^2 \cdot \gamma \cdot R) \tag{A.4}$$

$$\rho_3 = p_3/(T_3 \cdot R) \tag{A.5}$$

$$h_3 = C_p \cdot T_3 \tag{A.6}$$

$$a_3 = \sqrt{\gamma \cdot R \cdot T_3} \tag{A.7}$$

$$p_{03} = p_3 \cdot (1 + (\gamma - 1) \cdot M_3^2)^{\gamma/(\gamma-1)} \tag{A.8}$$

$$S_3 = C_p \cdot \log_{10}(T_3/T_{ref}) - R \cdot \log_{10}(p_3/p_{ref}) \tag{A.9}$$

Similar, for non-ideal gas, the functions are replaces by functions call or calls to appropriate property databases (e.g. CoolProp [27]) to recover all the required properties.

Appendix B. Models to calculate the total pressure loss η_p

In this context, the models to calculate the total pressure loss are listed as follows. First we assume the energy is conserved across the whole stage,

$$H_{01} = H_{03} = H_{04} \ . \tag{B.1}$$

Then we assume the flow within the stator is free of loss, i.e. the loss generates after the stator outlet section.

$$S_{01} = S_{03} \ . \tag{B.2}$$

Then from Fig. 7 of study [17], the entropy increment is ΔS_i and ΔS_4, and the entropy at rotor inlet section is

$$S_{04} = S_{03} + \Delta S_i + \Delta S_4 \ . \tag{B.3}$$

Hence, the total pressure at Section 4 p_{04} can be calculated using EoSs, calling H_{04} and S_{04},

$$p_{04} = \boldsymbol{f}(S_{04}, H_{04}) \ . \tag{B.4}$$

As we assume no total-pressure loss was within the stator passage, $p_{03} = p_{01}$, hence the total pressure loss coefficient η_p can be calculated through

$$\eta_p = \frac{p_{04}}{p_{04}} \ . \tag{B.5}$$

Appendix C. Overview of stator design models

C.1. Blade number

To design radial inflow turbine stator NGVs, the Z_s should correctly selected. Glassman [14] presented a model to calculate the Z_s based on the NGV blade solidity, σ,

$$\sigma = \frac{c}{s} \ . \tag{C.1}$$

The number of NGVs blades is calculated through

$$Z_s = \frac{2\pi r_1 \sigma}{c} \ , \tag{C.2}$$

where c is the NGV chord and s is the NGV blade spacing at blade-row exit. The blade chord, c can be calculated as

$$c = \sqrt{r_1^2 + r_3^2 - \sqrt{(r_1^2 + r_3^2)^2 - (r_1^2 - r_3^2)^2 / \cos^2\left(\frac{\alpha_1 + \alpha_3}{2}\right)}} \ . \tag{C.3}$$

The inlet radius is recommended in Table 1, that the inlet flow angle can be calculated as

$$\alpha_1 = \sin^{-1}\left(\frac{\sin\alpha_3}{1 + 0.2/\frac{r_3}{r_4}}\right). \tag{C.4}$$

As a recommendation, Glassman use the solidity value of σ = 1.35 to calculate the number of stator NGVs. A more recent study by Simpson [31] recommend the optimum of solidity value of 1.25. Some studies also presented models to determine the RIT NGVs blade solidity.

C.2. Blade solidity

Zweifel [32] gave a blade loading correlation to determine the optimum axial turbomachinery solidity, as

$$\psi = 2\left(\frac{s}{c}\right)\cos^2(\tan\alpha_2 - \tan\alpha_1) \tag{C.5}$$

Zweifel recommended an optimum value of ψ for the minimum loss to lie between 0.75 and 0.85. This optimum value relates to the axial turbine stages only. It is conventional in radial cascades to define the vane spacing at the trailing edge, since most of the flow turbine and acceleration takes place at this pitch circle diameter. Hence to make sure a strict similarity with the Zweifel coefficient defined for axial cascades, the solidity should be defined at the mean of vane inlet and outlet radii.

C.3. Rotor–stator interspace

There are multiple studies to analysis the effect of rotor–stator interspace and to present models for interspace calculation. Tunakov [33] presented an empirical relationship to define the flow path length of the fluid in the rotor–stator interspace normalised by the hydraulic diameter.

$$\frac{\Delta r}{b\sin\alpha_3} \approx 2.0 \tag{C.6}$$

where Δr is the radial distance (the length of the rotor–stator interspace, equal to $r_3 - r_4$) between the vane trailing edge and the rotor tip. Watanabe et al. [34] carried out tests on a series of straight stator vanes giving varying r_3/r_4 values of 1.03, 1.05, 1.1, and 1.15 used in conjunction with a common 200 mm tip diameter rotor, and found that the stator design giving a 10 mm rotor–stator interspace ($r_3/r_4 = 1.05$) led to the highest turbine efficiency. Simpson et al. [31] designed a series of NGVs using commercial blade modelling and numerical analysis tools to investigate the effects that the r_3/r_4 parameter and the vane solidity σ on radial turbine stage efficiency. Based on the numerical and experimental results, the aerodynamic optimum values of the rotor–stator interspace parameter r_3/r_4 was recommended to be 1.175.

C.4. Loss calculation

The performance for RIT stators are important, and some studies presented models to predict the losses generated in the stator. Rohlik [13] provided the models to calculate the stator kinetic loss. The loss was obtained by the equation

$$e_s = \frac{0.0076}{\cos\alpha_3 - 0.025}\left(1 + \frac{\cos\alpha_{st}}{0.7}\right) \tag{C.7}$$

$$\alpha_{st} = \frac{\alpha_1 + \alpha_3}{2} \tag{C.8}$$

where e_s is the 3D blade row loss ratio of the stator NGVs, α_{st} is the blade stagger angle. α_1 is the flow angle in stator inlet, which can be obtained through

$$\alpha_1 = \tan^{-1}\left[\frac{\sin\alpha_3}{4\left(\frac{h_3}{D_3}\right) + \cos\alpha_3}\right], \tag{C.9}$$

where h_3 is the passage height at stator outlet. Glassman [14] proposed the models for calculating the viscous loss of the stator.

$$e_{2D} = \frac{\psi_{ti}}{s\cos\alpha_3 - \delta'_{ti} - t} \tag{C.10}$$

$$e_{3D} = e_{2D}\left(\frac{A_{3D}}{A_{2D}}\right) \tag{C.11}$$

Detailed equations are listed in the study of Glassman [14]. Glassman also make a recommendation for stator loss coefficient with unpublished data, that $e_{3D} = 0.064$. Khalil et al. [35] conducted a study to determine experimentally and theoretically the losses in radial inflow turbine nozzles.

$$Y = \frac{1 - p_{03}/p_{01}}{1 - p_3/p_{01}} \tag{C.12}$$

$$\zeta = \frac{(p_{01}/p_{03})^{\frac{\gamma-1}{\gamma}} - 1}{(p_{01}/p_3)^{\frac{\gamma-1}{\gamma}} - 1} \tag{C.13}$$

Through solving multiple equations that presented in study [35], the overall loss coefficients can be determined. They concluded that the loss in the vaneless region comprises only a small part of the total loss and, as such, turbine performance is unlikely to be affected by the addition of a large vaneless space.

References

[1] J. Qi, T. Reddell, K. Qin, K. Hooman, I.H. Jahn, Supercritical CO2 radial turbine design performance as a function of turbine size parameters, J. Turbomach. 139 (8) (2017) 081008.
[2] K. Kapoor, K.K. Pandey, A. Jain, A. Nandan, Evolution of solar energy in India: A review, Renew. Sustain. Energy Rev. 40 (2014) 475–487.
[3] E. Nest, Why Concentrated Solar Power (CSP) beats Photovoltaic (PV) at less than 3 USD cents per kWh, 2020, https://energy-nest.com/concentrated-solar-power-csp-beats-photovoltaic-pv-less-3-usd-cents-per-kwh/.
[4] W. Stein, R. Buck, Advanced power cycles for concentrated solar power, Sol. Energy 152 (2017) 91–105.
[5] J.-M. Yin, Q.-Y. Zheng, Z.-R. Peng, X.-R. Zhang, Review of supercritical CO2 power cycles integrated with CSP, Int. J. Energy Res. 44 (3) (2020) 1337–1369.
[6] E.G. Feher, The supercritical thermodynamic power cycle, Energy Convers. 8 (2) (1968) 85–90.
[7] C.S. Turchi, Z. Ma, T.W. Neises, M.J. Wagner, Thermodynamic study of advanced supercritical carbon dioxide power cycles for concentrating solar power systems, J. Solar Energy Eng. 135 (4) (2013).

[8] T. Conboy, M. Carlson, G. Rochau, Dry-cooled supercritical CO2 power for advanced nuclear reactors, J. Eng. Gas Turbines Power 137 (1) (2015).
[9] T. Allison, J. Moore, R. Pelton, J. Wilkes, B. Ertas, Turbomachinery, in: K. Brun, P. Friedman, R. Dennis (Eds.), Fundamentals and Applications of Supercritical Carbon Dioxide (SCO_2) Based Power Cycles, Woodhead Publishing, The Officers' Mess Business Centre, Royston Road, Duxford, CB22 4QH, United Kingdom, 2017, pp. 147–215, Ch. 7.
[10] S.K. Cho, J. Lee, J.I. Lee, J.E. Cha, S-CO2 turbine design for decay heat removal system of sodium cooled fast reactor, in: Turbo Expo: Power for Land, Sea, and Air, Vol. 49873, American Society of Mechanical Engineers, 2016, V009T36A006.
[11] E. Sauret, A.S. Rowlands, Candidate radial-inflow turbines and high-density working fluids for geothermal power systems, Energy 36 (7) (2011) 4460–4467.
[12] J.J. Sienicki, A. Moisseytsev, R.L. Fuller, S.A. Wright, P.S. Pickard, Scale dependencies of supercritical carbon dioxide brayton cycle technologies and the optimal size for a next-step supercritical CO2 cycle demonstration, in: SCO2 Power Cycle Symposium, 2011.
[13] H.E. Rohlik, Analytical Determination of Radial Inflow Turbine Design Geometry for Maximum Efficiency, National Aeronautics and Space Administration, 1968.
[14] A.J. Glassman, Computer program for design analysis of radial-inflow turbines, 1976.
[15] C. Rodgers, Meanline performance prediction for radial inflow turbines, in: Von Karman Institute for Fluid Dynamics, VKI Lecture Series, Small High Pressure Ratio Turbines, Vol. 7, 1987.
[16] H. Moustapha, M.F. Zelesky, N.C. Baines, D. Japikse, Axial and Radial Turbines, Vol. 2, Concepts NREC Wilder, VT, 2003.
[17] J.A. Keep, I. Jahn, Numerical loss investigation of a small scale, low specific speed supercritical CO2 radial inflow turbine, J. Eng. Gas Turbines Power-Trans. Asme 141 (9) (2019) 091003.
[18] C.A.M. Ventura, P.A. Jacobs, A.S. Rowlands, P. Petrie-Repar, E. Sauret, Preliminary design and performance estimation of radial inflow turbines: An automated approach, J. Fluids Eng. 134 (3) (2012) 31102.
[19] B. Nick, Turbine design and analysis, 2019, [Online; accessed 30-10-2022]. URL https://drive.google.com/drive/folders/1zs4OpjB179Zboug5s4XyreZXMxXoWVVJ.
[20] C.A. De Miranda Ventura, Aerodynamic design and performance estimation of radial inflow turbines for renewable power generation applications, 2012.
[21] A.P. Wheeler, J. Ong, A study of the three-dimensional unsteady real-gas flows within a transonic ORC turbine, in: ASME Turbo Expo 2014: Turbine Technical Conference and Exposition, American Society of Mechanical Engineers Digital Collection, 2014.
[22] N. Woolley, A. Hatton, Viscous flow in radial turbomachine blade passages, in: Conference on Heat and Fluid Flow in Steam and Gas Turbine Plant, Coventry, England, 1973, pp. 175–181.
[23] R.H. Aungier, Turbine Aerodynamics : Axial-Flow and Radial-Inflow Turbine Design and Analysis, ASME Press, Place of publication not identified, 2006.
[24] W. Traupel, Thermische Turbomaschinen, Springer-Verlag, Berlin Heidelberg New York, 1977.
[25] M. Schobeiri, Turbomachinery Flow Physics and Dynamic Performance, Vol. 1, Springer, 2012.
[26] J.J. More, B.S. Garbow, K.E. Hillstrom, User guide for MINPACK-1, 1980.
[27] I.H. Bell, J. Wronski, S. Quoilin, V. Lemort, Pure and pseudo-pure fluid thermophysical property evaluation and the open-source thermophysical property library CoolProp, Ind. Eng. Chem. Res. 53 (6) (2014) 2498–2508.
[28] R. Span, W. Wagner, A new equation of state for carbon dioxide covering the fluid region from the triple-point temperature to 1100 K at pressures up to 800 MPa, J. Phys. Chem. Ref. Data 25 (6) (1996) 1509–1596.
[29] W. Shao, J. Yang, X. Wang, Z. Ma, Accuracy study and stability control of a property-table-based CFD strategy for modeling SCO2 compressors working near the critical point of the fluid, Appl. Therm. Eng. 183 (2021) 116222.
[30] ANSYS, Academic Research, ANSYS CFX User Guide, Release 17.1, 2016.
[31] A.T. Simpson, S.W. Spence, J.K. Watterson, Numerical and experimental study of the performance effects of varying vaneless space and vane solidity in radial turbine stators, J. Turbomach. 135 (3) (2013) 031001.
[32] O. Zweifel, The spacing of turbo-machine blading, especially with large angular deflection, Brown Boveri Rev. 32 (12) (1945) 436–444.
[33] A. Tunakov, Izvestiya vysshikh uchebnykh(in Russian, "Effect of the radual clearance on the operation of a centripetal gas turbine"), Zaved. Aviatsionnaya Tech. 4 (1960) 83–92.
[34] I. Watanabe, I. Ariga, T. Mashimo, Effect of dimensional parameters of impellers on performance characteristics of a radial-inflow turbine, J. Eng. Gas Turbines Power 93 (1) (1971) 81.
[35] I.M. Khalil, W. Tabakoff, A. Hamed, Losses in radial inflow turbines, J. Fluids Eng. Trans. ASME 98 (3) (1976) 364–371.